Supporting Information

Iridium Complexes and Clusters in Dealuminated Zeolite HY: Distribution between crystalline and impurity Amorphous Regions**

Claudia Martinez-Macias,[†] Pinghong Xu,[†] Son-Jong Hwang,[§] Jing Lu,[†] Cong-Yan Chen,[†,‡] Nigel D. Browning,[¬] and Bruce C. Gates*[,†]

[†] Department of Chemical Engineering and Materials Science, University of California, Davis, One Shields Avenue, Davis, CA 95616, United States

[¬] Fundamental and Computational Sciences, Pacific Northwest National Laboratory, 902 Battelle Boulevard, Richland, WA 99352, United States

[‡] Chevron Energy Technology Co., Richmond, CA 94708, United States

[§] Division of Chemistry and Chemical Engineering, California Institute of Technology, Pasadena, CA 91125, United States

X-ray Absorption Spectroscopy. X-ray absorption spectra were recorded at beam line MR-CAT at the Advanced Photon Source (APS) at Argonne National Laboratory. The storage ring electron energy and ring currents were 7.0 GeV and 105 mA, respectively. The cryogenic double-crystal Si(111) monochromator was detuned by 20% at the Ir L_{III} edge to minimize the effects of higher harmonics in the X-ray beam. The sample was loaded into a flow-through cell in a nitrogen-filled glovebox.[1] The mass of sample (approximately 250 mg) was chosen to give an absorbance of approximately 2.0 calculated at an energy 50 eV greater than the absorption of the Ir L_{III} edge (11215 eV). X-ray absorption spectra were recorded at atmospheric pressure and room temperature (298–303 K). Spectra of platinum foil as a reference compound were recorded simultaneously, with the foil present in a cell downbeam of the sample cell. Thus, the beam passed through an ion chamber, then through the cell containing the sample, next through a second ion chamber, subsequently through the reference cell containing the platinum foil, and finally through another ion chamber. The sample was scanned in the presence of helium flowing at 50 mL (NTP)/min. Data were recorded for 3 min to determine each spectrum; this time represents a compromise between data quality and frequency of data collection. In the analysis of the data, an average of 5 consecutive scans was used.

EXAFS Data Analysis. The analysis of the EXAFS data was carried out with the software ATHENA of the IFEFFIT[2] package and the software XDAP.[3] The spectrum was the average of five spectra. ATHENA was used for edge calibration, alignment and averaging of the scans, and XDAP was used for deglitching, background removal, normalization, and conversion of the data into an EXAFS (χ) file. A "difference-file" technique was applied with XDAP for determination of optimized fit parameters. The data were normalized by dividing the absorption intensity by the height of the absorption edge. The spectrum was processed by fitting a second-order polynomial to the pre-edge region and subtracting this from the entire spectrum. The functional that was minimized and the function used to model the data are given elsewhere.[4] The background was subtracted by using cubic spline routines. Reference backscattering amplitudes and phase shifts were calculated with the software FEEF7[5] from crystallographic data characterizing $Ir(CO)_2(acac)$[6], Ir–Al alloy, Ir–Si alloy, and IrO_2.[7] The fit models include the following contributions: $Ir–C_{CO}$, $Ir–O_{CO}$ (taking into account the multiple scattering that is characteristic of a linear Ir–C–O moiety),[8-9] $Ir–O_{zeolite}$, $Ir–Al_{zeolite}$, and $Ir–Si_{zeolite}$. Iterative fitting was performed with the unfiltered data until optimum agreement was attained between the calculated k^0-, k^1-, k^2-, and k^3-weighted EXAFS data and each postulated model (k is the wave vector). The data were fitted in distance (r) space with the Fourier-transformed χ data (r is the distance from the absorbing atom, and χ is the EXAFS function). To estimate the error in the data, the root mean square of the value obtained by the subtraction of smoothed χ data from the background-subtracted experimental values was calculated and used for the calculation of the goodness of fit according to the following expression:

$$goodness\ of\ fit = \frac{\nu}{NPTS(\nu - N_{free})} \sum_{i=1}^{NPTS} \left(\frac{\chi_{exp,i} - \chi_{model,i}}{\sigma_{exp,i}} \right)$$

where χ_{exp} and χ_{model} are the experimental and fit EXAFS respectively, σ_{exp} is the error in the experimental results, ν is the number of independent data points in the fit range, N_{free} is the number of free parameters, and NPTS is the number of data points in the fit range. The goodness of fit $(\Delta\chi)^2$ takes into account the number of fitted parameters and statistically independent data points, thus allowing comparisons of candidate models containing various numbers of contributions and fit ranges. By using $(\Delta\chi)^2$ we were able to determine whether the addition of each new contribution to a candidate model improved the fit. To calculate the $(\Delta\chi)^2$ parameter for each of the fits, an estimate of the error (or noise)

in the EXAFS data was calculated by Fourier filtering the data up to an R value of 5 Å. The justified number of parameters used in the fitting was calculated from the Nyquist theorem:[10] $n = \left(\frac{2\Delta k \Delta r}{\pi}\right) + 2$, where Δk and Δr are the k and r ranges used in the fitting.

Statistical justification of Models I and II:

Model I includes the following contributions, each expected on the basis of the reported chemistry of comparable samples: Ir–$O_{zeolite}$, Ir–C_{CO}, Ir–O_{CO} and Ir–$Al_{zeolite}$. Each of these contributions was fitted by using the best combination of reference files. The results characterizing the fit parameters obtained with Model I are summarized in Table S-1. Figure S8 shows the results of the EXAFS data analysis. The k-range for the fit is from 4.19 to 11.84 $Å^{-1}$, and the r-range is from 0 to 3 Å. The Nyquist theorem indicates that the number of statistically justified fit parameters is 17, which exceeds the number used in fitting (16) with this model.

Model II includes the following contributions: Ir–$O_{zeolite}$, Ir–C_{CO}, Ir–O_{CO}, Ir–$Al_{zeolite}$, and Ir–$Si_{zeolite}$. Each of these contributions was fitted by using the best combination of reference files. The results characterizing the fit parameters obtained with Model II are summarized in Table S-1. Figure S9 shows the results of the EXAFS data analysis for the data set characterizing the sample. The k-range for the fit is from 4.19 to 11.84 $Å^{-1}$, and the r-range is from 0 to 4 Å. The Nyquist theorem indicates that the number of statistically justified fit parameters is 21, which exceeds the number used in fitting (20) with this model.

Comparing Model I and Model II, we see that the fit of the data with each shows that the sample incorporates mononuclear iridium bonded to 2 carbonyls ligands and to oxygen atoms of the support. The overall fit is better for Model II, as stated by a lower goodness of fit (18.7 for Model I and 4.5 for Model II). Therefore, Model II was chosen as the best fit. We reemphasize that the most important and most precisely determined fit parameters are essentially independent of the model.

Table S-1. Summary of EXAFS fit parameters[a] characterizing $Ir(CO)_2$ bonded to dealuminated zeolite HY. EXAFS data collected at 300 K and 1 bar with sample in helium flowing at 50 mL(NTP)/min.

Model	Shell	*N*	*R*(Å)	$10^3 \times \Delta\sigma^2$ (Å^2)	ΔE_0 (eV)	*k*-range [Å^{-1}]	*r*-range [Å]	*Goodness of fit*
I	$Ir–O_{zeolite}$	2.2	2.06	7.9	4.6	4.19 – 11.84	0–3	18.7
	$Ir–C_{CO}$	1.9	1.87	10.9	5.2			
	$Ir–O_{CO}$	1.9	2.97	10.9	-6.6			
	$Ir–Al_{zeolite}$	1.0	2.99	1.1	-6.7			
II	$Ir–O_{zeolite}$	2.2	2.07	9.3	1.7	4.19 – 11.84	0–4	4.5
	$Ir–C_{CO}$	1.9	1.85	10.6	6.7			
	$Ir–O_{CO}$	1.9	2.96	8.8	-4.9			
	$Ir–Al_{zeolite}$	0.8	2.99	0.4	-7.1			
	$Ir–Si_{zeolite}$	2.8	3.46	10.6	-7.5			

[a] Notation: *N*, coordination number; *R*, distance between absorber and backscatterer atoms; $\Delta\sigma^2$, disorder term (Debye-Waller factor); ΔE_0, inner potential correction. Error bounds characterizing the structural parameters obtained by EXAFS spectroscopy are estimated to be as follows: $N \pm 20\%$; $R \pm 0.02$ Å; $\Delta\sigma^2 \pm 20\%$; and inner potential correction $\Delta E_0 \pm 20\%$. The errors in the Ir–Al and Ir–Si contributions are larger than those characterizing the other contributions, and a basis for estimates of the uncertainties in these values is not provided by the data.

Analysis of MAS–NMR SPECTRA: The atomic Si:Al ratio of this sample was found by elemental analysis to be 27.4. If this sample were defect free, the integration of the -102-ppm peak should theoretically give the value of 14.6, reflecting that in such a case there are 27.4 atoms for each Al atom which is bound to 4 Si atoms and, therefore, 4 of 27.4 atoms (namely, 4/27.4 = 14.6%) belong to the $Si(OAl)(OSi)_3$ sites. For any defect-containing samples, the difference in integration of the -102 ppm peak from 14.6 is assigned to the contribution from the defect sites (Q^3). According to Figure S4, ~21% (namely, (18.5 - 14.6)/18.5) of the -102 ppm peak of the Ir-containing Y zeolite are Q^3 Si atoms, indicating that $Q^3/(Q^4 + Q^3)$ is ~5%. Note that the NMR spectra reported here for the iridium-containing zeolite are nearly indistinguishable from those of the precursor material (dealuminated zeolite HY, not shown) with the exception of a minor change in the Q^3 ratio, indicating no change in the zeolite framework after the iridium loading.

Analysis of CPMAS-NMR SPECTRUM: The spectrum (Figure S4B) shows selectively the -102 ppm peak, Q^3 ($\equiv HOSi(OSi)_3Si$), as well as a peak at -92 ppm attributed to Q^2 species ($\equiv(HOSi)_2(OSi)_2Si$) which is also related to internal defect sites. The broadness of the peaks is associated with the presence of amorphous material. Figure S4C shows the spectral deconvolution of the ^{29}Si CPMAS-NMR spectrum with peaks at -107, -102, and -92 ppm; the broadness of the peaks is associated with the presence of amorphous material, approximately 10%.

STEM analysis: Beam effects were analyzed by taking sequential images, Figure 4 in the main text, in which it is evident that the iridium located inside the zeolite cages was resistant to aggregation, because, we infer, of pore confinement. On the other hand, the iridium located in the amorphous region, present already as clusters in the first image taken at < 5 s of beam exposure, started to aggregate further after 10 s. Nonetheless, the sizes of the clusters present in the first image, with a mean diameter of 0.60 ± 0.18 nm, are great enough to rule out the possibility of cluster formation resulting from beam exposure because the time required for the iridium to form clusters of that size is greater than 5 s.

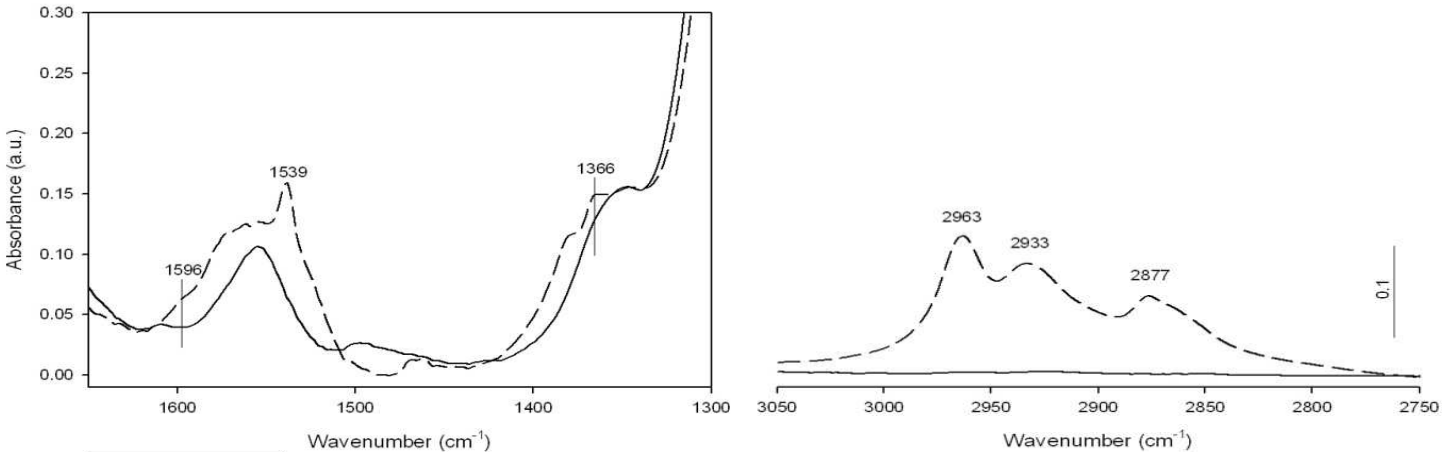

Figure S1. IR spectra characterizing the bare zeolite (solid line) and the zeolite after contact with $Ir(CO)_2(acac)$ (dashed line).

In Figure S1 there are bands at 2963, 2933, and 2877 cm^{-1}, assigned to $\nu_{(CH3)}$ vibrations of the acac, and bands at 1596, 1539, and 1366 cm^{-1}, assigned to ν_{COring}, ν_{C-C-Cs}, and δ_{CH}, respectively. These results imply that after the acac had been dissociated from the $Ir(CO)_2(acac)$, the acac adsorbed on the zeolite, as was observed in previous work.[11]

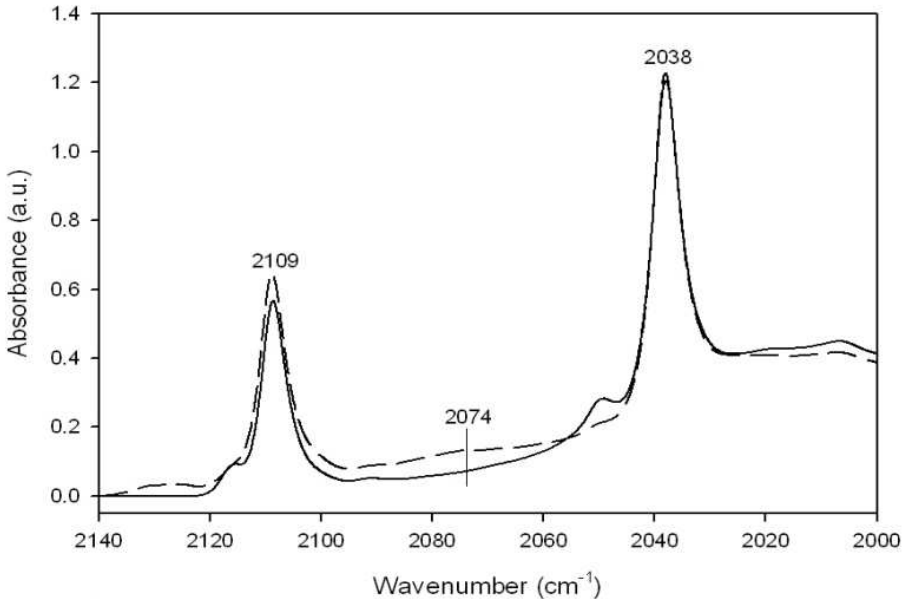

Figure S2. IR spectra characterizing zeolite-supported $Ir(CO)_2$ in flowing helium (solid line) and after exposure to a pulse of CO (dashed line).

Figure S2 shows the IR spectrum of the sample after contact with a CO pulse (10% CO in helium) to determine whether there was any indication of cluster formation that might have occurred during synthesis of the supported iridium complex. After the CO pulse, the only change was the appearance of a band at 2074 cm^{-1}, assigned to iridium tricarbonyl.[12-13] The sharpness of the bands and the lack of any band indicating the presence of bridging carbonyls demonstrate the high degree of uniformity of the sample and give no evidence of the presence of iridium clusters.

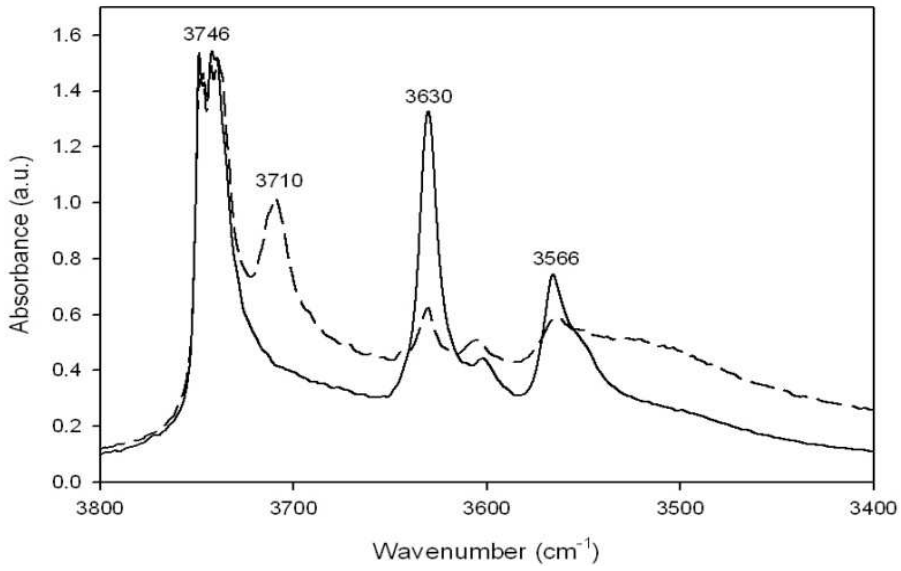

Figure S3. IR spectra characterizing the bare zeolite before treatment (solid line) and after treatment in helium for 2 h 45 min at room temperature.

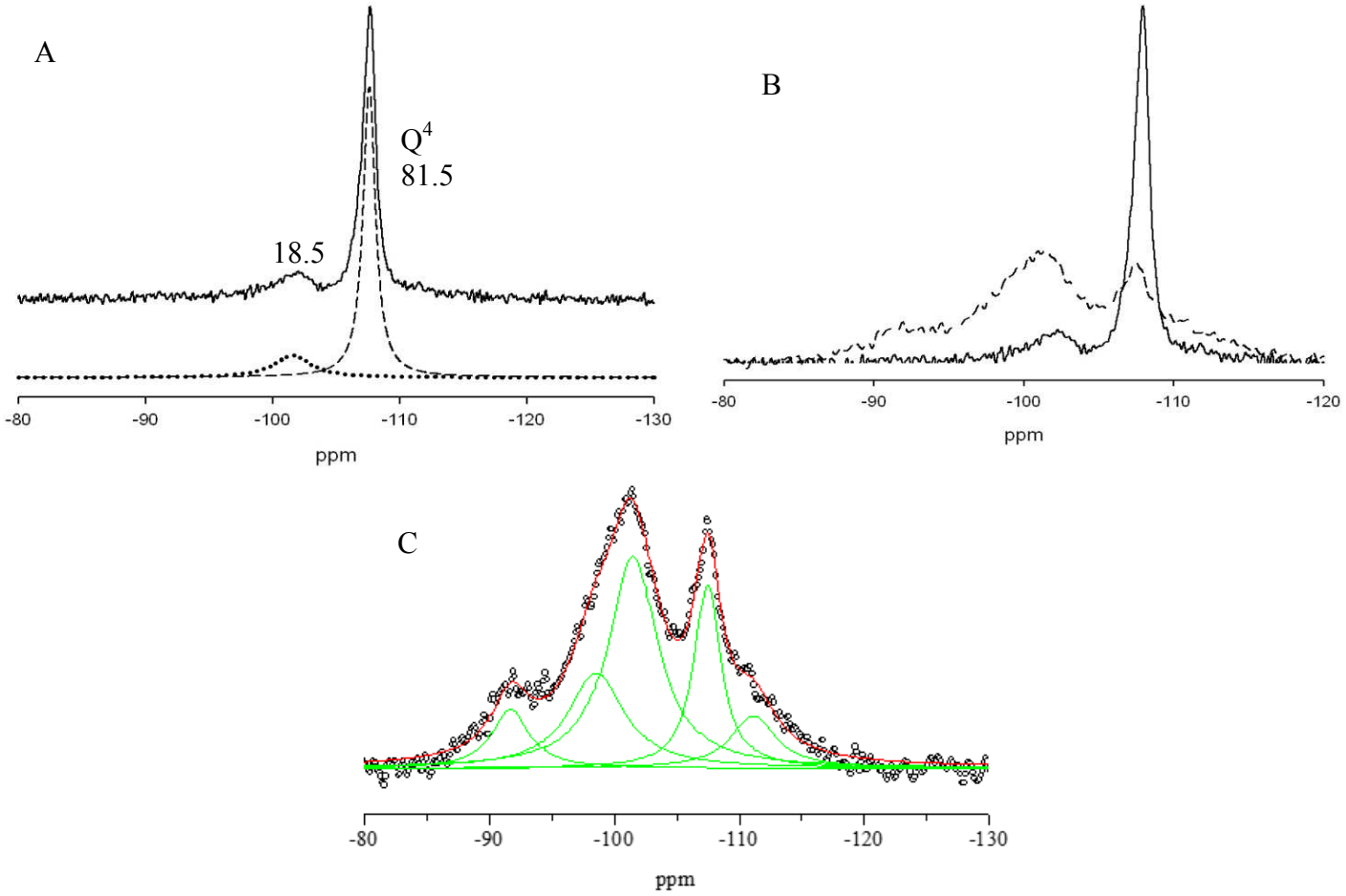

Figure S4. (A) ^{29}Si MAS-NMR spectrum of the zeolite after contact with $Ir(CO)_2(acac)$ (solid line), spectral deconvolution of -102 ppm peak (dotted line) and spectral deconvolution of -107 ppm peak (dashed line). The peak areas for -102:-107 ppm peaks are 18.5:81.5 respectively. The identity of these peaks is discussed in MAS-NMR section. (B) ^{29}Si MAS-NMR spectrum of the zeolite after contact with $Ir(CO)_2(acac)$ (solid line) and ^{29}Si CPMAS-NMR spectrum of the same sample with CP contact time of 2.0 ms at 8 kHz spinning rate (dashed line). (C) ^{29}Si CPMAS NMR spectrum of the same sample with CP contact time of 2.0 ms at 8 kHz spinning rate (dotted line) and spectral deconvolution of -95, -102 and -107 ppm peaks (green solid line)

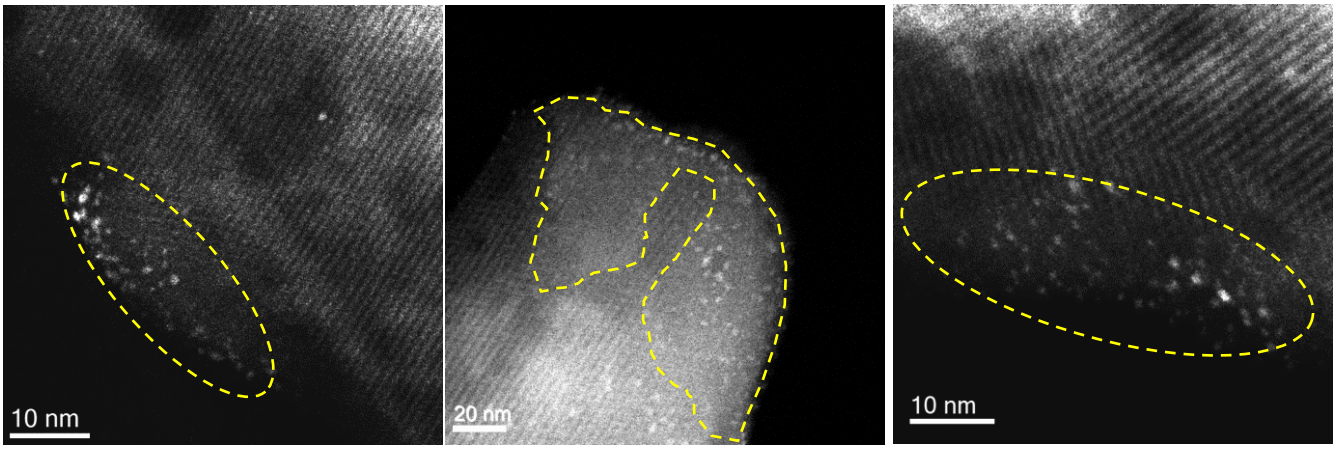

Figure S5. Aberration-corrected HAADF-STEM image of dealuminated HY zeolite containing $Ir(CO)_2$ (1 wt% iridium) showing the zeolite framework in the [110] direction. The regions encircled in yellow are amorphous regions.

The amorphous region and the crystalline region can be distinguished as separate regions as shown in Figure S5. Furthermore, the high contrast between the pores and the nearby zeolite framework gives evidence that there is almost no amorphous material located in the channels of the crystalline framework.

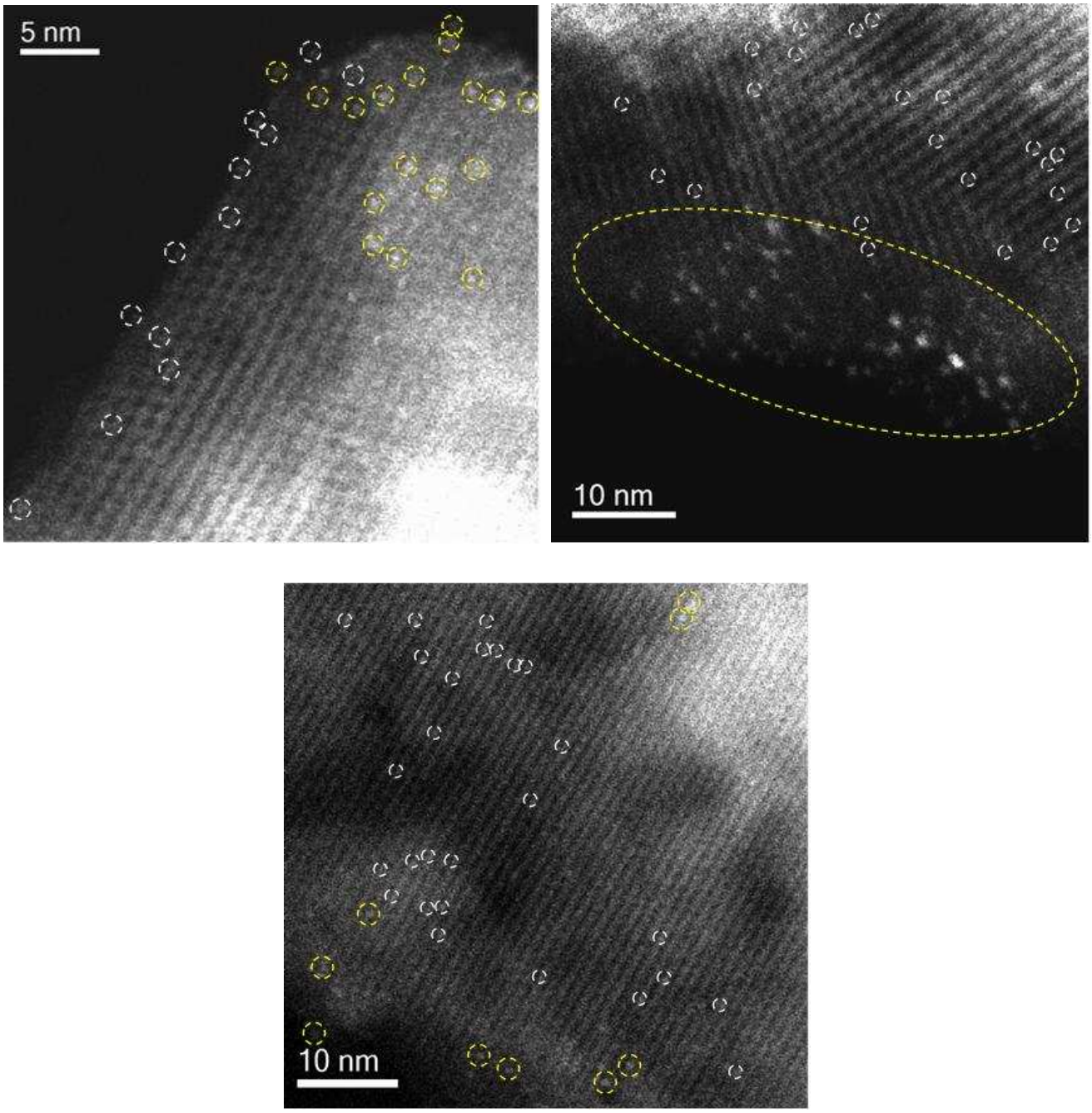

Figure S6. HAADF-STEM images of $Ir(CO)_2$/HY zeolite at various positions, showing Ir atoms in mononuclear iridium complexes in the crystalline region of the zeolite (bright features in white) and clusters in the amorphous region (bright features in yellow).

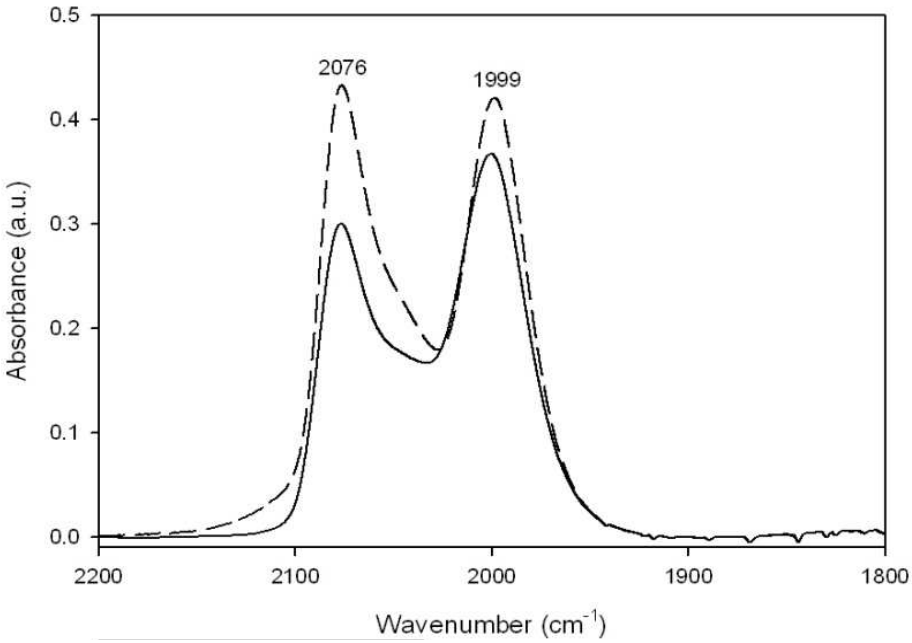

Figure S7. IR spectra characterizing γ-Al_2O_3-supported $Ir(CO)_2$ in flowing helium (solid line) and after exposure to a pulse of CO (dashed line). The bands are broader than those in the zeolite, corresponding to the lower degree of uniformity of the iridium complexes in the amorphous support.

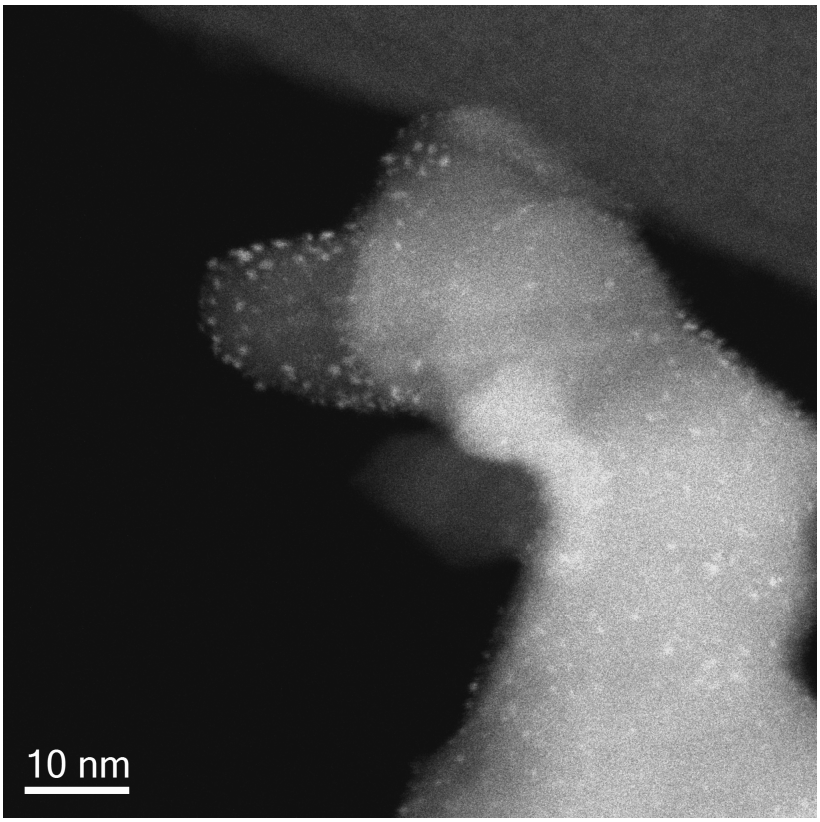

Figure S8. HAADF-STEM image of sample formed from $Ir(CO)_2(acac)$ in contact with γ-Al_2O_3.

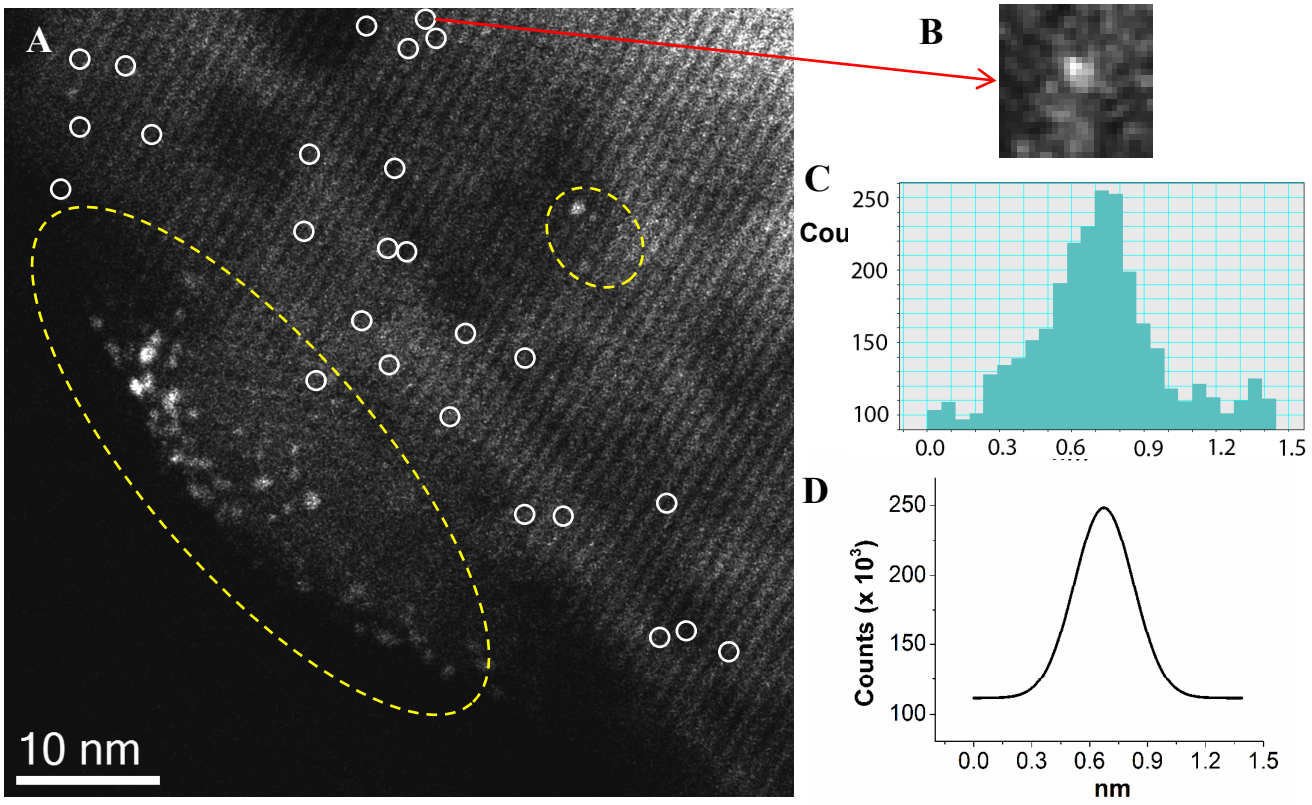

Figure S9. Example illustrating high signal-to-noise ratio (SNR) of mononuclear iridium species. (A) Aberration-corrected HAADF-STEM image of HY zeolite containing $Ir(CO)_2$ (1 wt% iridium) showing the zeolite framework in the [110] direction. Bright features in white circles are examples of site-isolated mononuclear iridium complexes in the zeolite framework; those in yellow circles are iridium clusters in amorphous regions. (B) Enlarged image of the example mononuclear iridium complexes, with a line drawn across the top for generation of the intensity profile shown in (C) using Digital Micrograph (Gatan). (D) Gaussian fit of the example mononuclear iridium complexes using OrginPro.

The STEM images show the presence of mononuclear iridium species with large single-to-noise ratio (SNR), as illustrated for one of the Ir atoms in Figure S9 (A-C). The intensity of signal characterizing the Ir atom shows a Gaussian distribution, as expected. The signal characterizing this mononuclear iridium species is approximately 1.5 times that of the background signal from the zeolite framework (consisting of tens of unit cells). Such a strong local signal could not be explained by artifacts in the images, such as locally different densities of the zeolite framework, or random noise in the STEM images from the CCD detector, or optical defects generated during electron-beam scanning. Some distortion of the STEM images would be expected, mainly because of sample drift during image acquisition, which might result in distortion of the images of the pores, which could in prospect make it difficult to locate metal species in the zeolite framework in extreme cases. However, such potential problems are now addressed routinely in STEM imaging (and in our work) and are not a concern.

Furthermore, STEM images of the iridium-containing zeolite recorded after various times of exposure to the electron beam (up to 86 s) have been recorded (Figure 4 in the main text), during which no evidence of large zeolite framework density differences or significant optical defect generation during electron-beam scanning were evident. The fact that both the mononuclear iridium species and iridium clusters were clearly observed at nearly the same locations cannot be explained by random noise of the STEM images from the CCD detector.

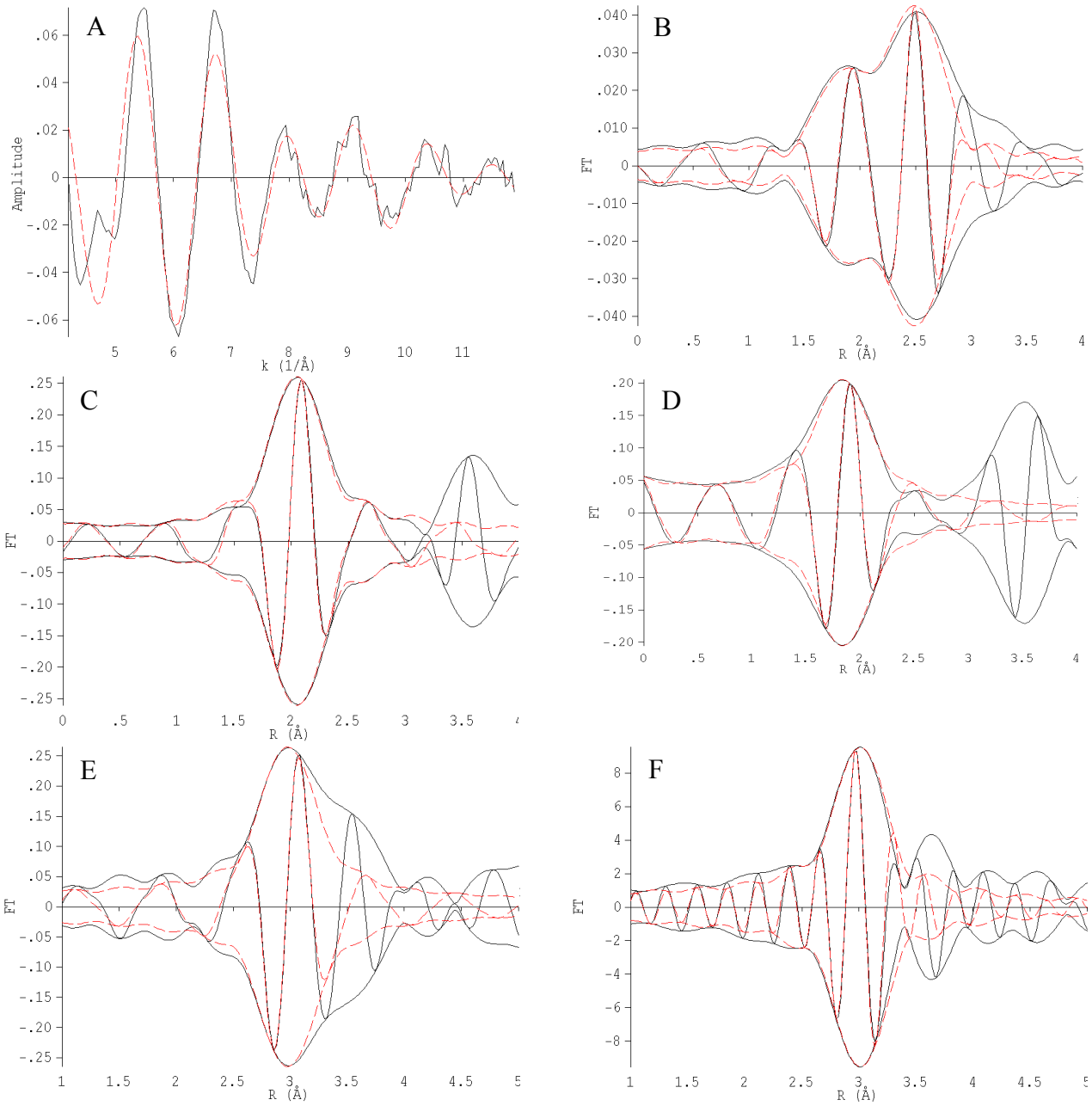

Figure S10. EXAFS data characterizing dealuminated zeolite-supported iridium complex formed by absorption of $Ir(CO)_2(acac)$ on the zeolite (Model I). The spectra were recorded with the sample in flowing helium at 300 K. (A) k^1-weighted EXAFS function, $k^1(\chi)$ (solid line) and sum of the calculated contributions (dashed line); (B) k^1-weighted imaginary part and magnitude of the Fourier transform of the data (solid line) and sum of the calculated contributions (dashed line); (C) k^1-weighted, phase-corrected, imaginary part and magnitude of the Fourier transform of the data (solid line) and calculated contributions (dashed line) of Ir-$O_{zeolite}$ shell; (D) k^1-weighted, phase-corrected, imaginary part and magnitude of the Fourier transform of the data (solid line) and calculated contributions (dashed line) of Ir-C_{CO} shell; (E) k^1-weighted, phase-corrected, imaginary part and magnitude of the Fourier transform of the data (solid line) and calculated contributions (dashed line) of Ir-O_{CO} shell; (F) k^3-weighted, phase-corrected, imaginary part and magnitude of the Fourier transform of the data (solid line) and calculated contributions (dashed line) of Ir-$Al_{zeolite}$ shell.

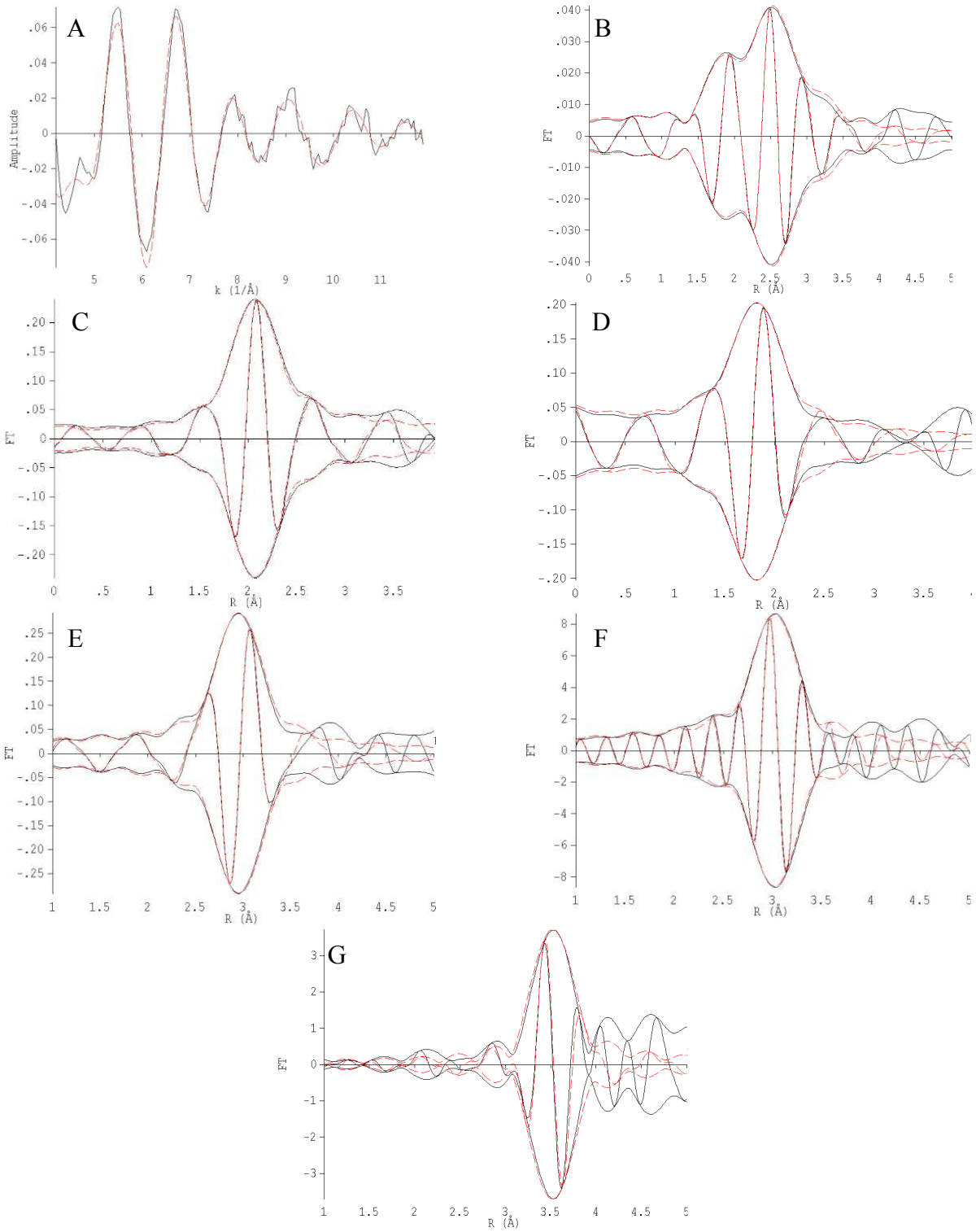

Figure S11. EXAFS data characterizing dealuminated zeolite-supported iridium complex formed by absorption of $Ir(CO)_2(acac)$ on the zeolite (Model II). The spectra were recorded with the sample in flowing helium at 300 K. (A) k^1-weighted EXAFS function, $k^1(\chi)$ (solid line) and sum of the calculated contributions (dashed line); (B) k^1-weighted imaginary part and magnitude of the Fourier transform of the data (solid line) and sum of the calculated contributions (dashed line); (C) k^1-weighted, phase-corrected, imaginary part and magnitude of the Fourier transform of the data (solid line) and calculated contributions (dashed line) of Ir-$O_{zeolite}$ shell; (D) k^1-weighted, phase-corrected, imaginary part and magnitude of the Fourier transform of the data (solid line) and calculated contributions (dashed line) of Ir-C_{CO} shell; (E) k^1-weighted, phase-corrected, imaginary part and magnitude of the Fourier transform of the data (solid line) and calculated contributions (dashed line) of Ir-

O_{CO} shell; (F) k^3-weighted, phase-corrected, imaginary part and magnitude of the Fourier transform of the data (solid line) and calculated contributions (dashed line) of Ir-$Al_{zeolite}$ shell, (G) k^3-weighted, phase corrected, imaginary part and magnitude of the Fourier transform of the data (solid line) and calculated contributions (dashed line) of Ir-$Si_{zeolite}$ shell.

[1] Odzak J. F.; Argo A. M.; Lai F. S.; Gates B. C.; Pandya K.; Feraria L.; *Rev. Sci. Instrum.* **2001**, *72*, 3943-3945.
[2] Neville M.; *J. Synchrotron Rad.* **2001**, *8*, 322-324.
[3] Vaarkamp M.; Linders J. C.; Koningsberger D. C.; *Physica B* **1995**, 209, 159-160.
[4] Koningsberger D. C.; Mojet B. L.; van Dorssen G. E.; Ramaker D. E.; *Top Catal.* **2000**, *10*, 143-155.
[5] Zabinsky S. E.; Rehr J. J.; Ankudinov A.; Albers R. C.; Eller M. J.; *Phys. Rev. B.* **1995**, *52*, 2995-3009.
[6] Zherikova K. V.; Kuratieva N. V.; Morozova N. B.; *J. Struct Chem* **2009**, *50*, 574-576.
[7] Pearson W. B.; Calvert L. D.; Villars P.; *Pearson's Handbook of Crystallographic Data for Intermetallic Phases*, American Society for Metals, Ohio, **1985**.
[8] van Zon F. B. M.; Kirlin P. S.; Gates B. C.; Koningsberger D. C.; *J. Phys. Chem.* **1989**, *93*, 2218-2222.
[9] Duivenvoorden F. B. M.; Koningsberger D. C.; Uh Y. S.; Gates B. C.; *J. Am. Chem. Soc.* **1986**, *108*, 6254-6262.
[10] Lytle F. W.; Sayers D. E.; Stern E. A.; *Physica B* **1989**, *158*, 701-722.
[11] Uzun A.; Bhirud V. A.; Kletnieks P. W.; Haw J. F.; and Gates B. C.; *J. Phys. Chem. C* **2007**, *111*, 15064-15073.
[12] Lu J.; Serna P. and Gates B. C.; *ACS Catal.* **2011**, *1*, 1549-1561.
[13] Mihaylov M.; Ivanova E.; Thibault-Starzyk F.; Daturi M.; Dimitrov L.; Hadjiivanov K. I.; *J. Phys. Chem. B* **2006**, *10*, 10383-10389.